Nanoscale

PAPER

Cite this: *Nanoscale*, 2016, **8**, 16387

Flexible hierarchical membranes of WS_2 nanosheets grown on graphene-wrapped electrospun carbon nanofibers as advanced anodes for highly reversible lithium storage†

Longsheng Zhang,[a] Wei Fan*[b] and Tianxi Liu*[a,b]

Received 25th May 2016,
Accepted 19th August 2016

DOI: 10.1039/c6nr04241d

www.rsc.org/nanoscale

It is still very challenging to achieve effective combination of carbon nanofibers and graphene sheets. In this study, a novel and facile method is developed to prepare flexible graphene/carbon nanofiber (GCNF) membranes with every carbon nanofiber wrapped by conductive graphene sheets, resulting in a remarkable improvement of their electrical conductivity. This method only entails a moderate process of soaking the pre-oxidized electrospun polyacrylonitrile (oPAN) nanofiber membranes in graphene oxide (GO) aqueous dispersion, and subsequent carbonization of the GO/oPAN hybrid membranes. By using the highly conductive GCNF membrane as a template, hierarchical WS_2/GCNF hybrid membranes with few-layer WS_2 nanosheets uniformly grown on GCNF nanofibers were fabricated as high-performance anodes for lithium ion batteries. Benefiting from the synergistic effects of GCNF nanofibers and WS_2 nanosheets, the resulting WS_2/GCNF hybrid membranes possessed a porous structure, large specific surface area, high electrical conductivity and good structural integrity, which are favorable for the rapid diffusion of lithium ions, fast transfer of electrons and overall electrochemical stability. As a result, the optimized WS_2/GCNF hybrid membrane exhibited a high initial charge capacity of 1128.2 mA h g^{-1} at a current density of 0.1 A g^{-1} and outstanding cycling stability with 95% capacity retention after 100 cycles.

1. Introduction

The continuously aggravating energy and environmental crisis have put forward the development of efficient energy storage devices, such as supercapacitors, lithium-ion batteries, solar cells and fuel cells.[1] Among them, lithium ion batteries (LIBs) have received tremendous attention owing to their high energy density, long cycling life and environmental benignity, which have become one of the prominent power sources for portable electronics and electric vehicles.[2] Currently, graphite is the most widely used anode material in commercialized LIBs; but it cannot meet the requirements for next-generation LIBs due to its low theoretical specific capacity (372 mA h g^{-1}).[3] Therefore, in order to push the energy density limit of LIBs, alternative anode materials with high specific capacity and good cyclic stability are strongly desired.[4]

Recently, a variety of layered transition-metal dichalcogenides (LTMDs) have been extensively studied as promising anode materials for next-generation LIBs owing to their high theoretical specific capacities and two-dimensional layer structures.[5] As a typical type of LTMDs, tungsten disulfide (WS_2) has a similar structure to graphite, consisting of three-atom layers (S–W–S) stacked together through weak van der Waals interactions.[6] Notably, the interlayer spacing (0.64 nm) of WS_2 is much larger than that of graphite (0.34 nm), which can ensure easy intercalation/deintercalation of lithium ions and lead to significantly improved lithium storage performance.[7] However, the practical application of WS_2 for LIBs is severely hampered by its poor electrical conductivity and large volume expansion/contraction during the lithiation/delithiation processes, resulting in inferior structural stability and rapid capacity fading.[8] To overcome these problems, one effective approach is to optimize the WS_2 materials to nanostructures and construct composites of WS_2 dispersed in a conductive matrix such as graphene, amorphous carbon or carbon nanotubes.[9–11] On the one hand, reducing the size of WS_2 materials to the nanoscale can effectively mitigate the volumetric expansion/contraction from the Li^+ insertion/extraction

[a]*State Key Laboratory of Molecular Engineering of Polymers, Department of Macromolecular Science, Fudan University, 220 Handan Road, Shanghai 200433, P. R. China. E-mail: txliu@fudan.edu.cn, txliu@dhu.edu.cn*
[b]*State Key Laboratory for Modification of Chemical Fibers and Polymer Materials, College of Materials Science and Engineering, Donghua University, 2999 North Renmin Road, Shanghai 201620, P. R. China. E-mail: weifan@dhu.edu.cn*
†Electronic supplementary information (ESI) available. See DOI: 10.1039/c6nr04241d

processes, leading to less structural destruction and pulverization.[12] On the other hand, the carbonaceous matrixes can not only provide highly conductive pathways for rapid charge transfer, but play a structural buffering role in accommodating the interior strain caused by the volume changes of WS_2 materials during the lithiation/delithiation process.[13] For example, Du *et al.* synthesized WS_2/graphene hybrids with double carbon-coated WS_2 nanosheets that exhibited a high capacity of 486 mA h g^{-1} at a current density of 0.5 A g^{-1} with 90% capacity retention after 200 cycles.[14] Similarly, composites of WS_2 nanosheets confined within porous graphene frameworks delivered a capacity of 766 mA h g^{-1} at a current density of 0.1 A g^{-1} with negligible capacity fading after 100 cycles.[15] Nevertheless, these WS_2-based anode materials need to be mixed with polymer binders and conductive additives for battery tests, which are complicated and time-consuming. Besides, the polymer binders are insulating and electrochemically inert, which may severely block the diffusion channels of ion transportation and impair the overall electrochemical performance.[16]

To address these issues, a proper self-standing template with excellent electrical conductivity and structural stability for fabricating binder-free WS_2-based anode materials are needed for further improving their lithium storage performance. In particular, extensive studies have proved that electrospun carbon nanofiber (CNF) membranes are ideal matrixes owing to their unique three-dimensional (3D) nanofiber networks, large specific surface area, outstanding structural stability and mechanical flexibility.[17–19] Besides, electrospinning is a facile and efficient technique for preparing self-standing nanofiber membranes, which can effectively avoid the tedious preparation process of electrodes by using polymer binders and conductive additives.[20] Until now, various CNF-based anode materials (*e.g.* MoS_2/CNF, SnS_2/CNF and NiS/CNF) have been reported previously, resulting in greatly enhanced electrochemical performance.[21–23] However, given the relatively low electrical conductivity of the CNF membrane, the lithium storage performance of CNF-based anodes is still limited. Compared with CNF, graphene sheets possess significantly higher electrical conductivity that can greatly improve the electrical properties of the host materials after they are combined with other materials to form hybrid structures.[24] To the best of our knowledge, only a few efforts have been devoted to the combination of conductive graphene sheets and CNF membranes. Unfortunately, those works about CNF/graphene composites either involves complex techniques such as simultaneous electrospray/electrospinning,[25] or a conventional direct co-electrospinning process that cannot control the dispersion of graphene sheets and subsequently undermined the spinning stability.[26] It still remains very challenging to develop a facile and efficient assembly method to achieve effective combination of graphene sheets and electrospun CNF membranes.

In this work, we report a novel and efficient method to prepare a flexible hybrid membrane (GCNF membrane) of electrospun CNF wrapped by conductive graphene sheets. As illustrated in Fig. 1, the GCNF membranes are facilely prepared through a moderate process of soaking the pre-oxidized electrospun polyacrylonitrile (oPAN) nanofiber membranes in a graphene oxide (GO) aqueous dispersion and subsequent carbonization of the GO/oPAN hybrid membranes. The resulting GCNF membrane possesses a 3D porous structure, large surface area and excellent electrical conductivity, which was employed as a self-standing template to fabricate hierarchical WS_2/GCNF hybrid membrane of WS_2 nanosheets uniformly grown on GCNF nanofibers. The highly conductive graphene sheath of GCNF nanofibers can not only provide efficient transport of electrons for fast reaction of WS_2 nanosheets, but also maintain the overall structural integrity by mitigating their volumetric expansion/contraction during long-term cycling processes. Moreover, the 3D porous nanofiber networks of WS_2/GCNF hybrid membranes can effectively facilitate the rapid diffusion of lithium ions throughout the whole electrode structure to ensure sufficient contact and fast lithiation/delithiation with WS_2 nanosheets. As a result, the optimized WS_2/GCNF hybrid membrane delivers a high capacity of 1128.2 mA h g^{-1} at a current density of 0.1 A g^{-1}, and outstanding cycling stability with 95% capacity retention after 100 cycles, showing great potential as a binder-free anode material for high-performance LIBs.

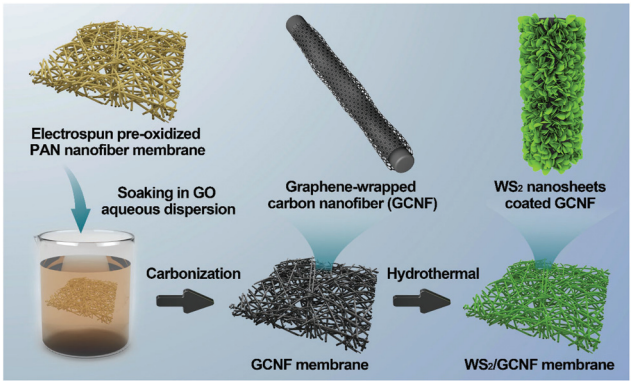

Fig. 1 Schematic of the preparation of flexible WS_2/GCNF hybrid membranes.

2. Experimental section

2.1. Materials

Polyacrylonitrile (PAN) (M_w = 150 000 g mol^{-1}) was purchased from Sigma-Aldrich. Natural graphite powder (325 mesh) was purchased from Alfa-Aesar. All the other reagents were purchased from Sinopharm Chemical Reagent Co. Ltd and used as received without further purification. Deionized (DI) water was used throughout all the experiments.

2.2. Preparation of graphene-wrapped CNF hybrid membranes

The preparation process of graphene-wrapped CNF (GCNF) hybrid membranes is illustrated in Fig. 1. The PAN nanofiber membrane was first prepared through a facile single-nozzle

electrospinning technique using a commercial electrospinning system (UCALERY Beijing Co., Ltd, China). Typically, 1 g PAN was dissolved in 5 mL DMF at room temperature under vigorous stirring to form a viscous transparent solution and then transferred into a 5 mL plastic syringe. The electrospinning process was carried out at an applied voltage of 20 kV with a feeding rate of 0.3 mm min^{-1} through a stainless steel needle positioned 20 cm away from the aluminum drum collector. To obtain oPAN membranes, the generated PAN nanofiber membrane was pre-oxidized at 250 °C in air atmosphere for 2 h with a heating rate of 1 °C min^{-1}. Graphene oxide (GO) was synthesized from natural graphite powder by a modified Hummers method.[27] The resulting GO solid was dispersed in water by ultrasonication for 30 min to make a homogeneous GO aqueous dispersion. Then, the oPAN membranes were immersed in the GO aqueous suspension (2 mg mL^{-1}) at room temperature for 24 h to ensure sufficient contact and interactions between GO sheets and oPAN nanofibers. The as-fabricated GO/oPAN membranes were rinsed with absolute ethanol several times to remove residual GO and water. Finally, the GO/oPAN membranes were dried under vacuum and then carbonized in a conventional tube furnace at 950 °C for 2 h in N_2 atmosphere to obtain GCNF membranes.

2.3. Preparation of WS_2/GCNF hybrid membranes

The WS_2/GCNF hybrid membranes was prepared *via* a facile one-step solvothermal method. Typically, a certain amount of $(NH_4)_2WS_4$ (5 mg, 10 mg and 20 mg, respectively) was dissolved in 20 mL DMF solution under stirring to form a homogeneous solution. Then, the as-prepared GCNF membranes were immersed in the above mixture solution, transferred in a 45 mL Teflon-lined stainless steel autoclave and maintained at 220 °C for 12 h to grow WS_2 nanosheets on GCNF nanofibers. After the reaction cooled down to room temperature naturally, the membranes were washed with water several times and dried at 60 °C under vacuum. Notably, the content of WS_2 nanosheets in the WS_2/GCNF hybrid membranes was readily tunable by adjusting the concentrations of $(NH_4)_2WS_4$ during the preparation procedure. Correspondingly, the WS_2/GCNF hybrid membranes thus prepared with increasing $(NH_4)_2WS_4$ concentrations were named as WS_2/GCNF-1, WS_2/GCNF-2 and WS_2/GCNF-3, respectively. Besides this, three WS_2/CNF hybrid membranes with increasing content of WS_2 nanosheets directly grown on CNF membranes were also prepared *via* the same solvothermal method, which were named as WS_2/CNF-1, WS_2/CNF-2 and WS_2/CNF-3, respectively. For the control experiment, bare WS_2 was prepared through the same procedure without addition of CNF or GCNF membranes.

2.4. Material characterization

Field emission scanning electron microscopy (FESEM) characterization was conducted with an Ultra 55 Zeiss FESEM at an accelerating voltage of 5 kV. Transmission electron microscopy (TEM) and high-resolution transmission electron microscopy (HRTEM) observations were performed with a Tecnai G2 20 TWIN TEM under an acceleration voltage of 200 kV. All the TEM samples were firstly dispersed in aqueous solutions *via* sonication to form homogenous suspensions. Then, the TEM samples were prepared by dropping the suspensions onto copper grids and drying in air. Atomic force microscopy (AFM) images were taken under tapping mode with a Scanning Probe Microscope Nanoscope IV from Digital Instruments. X-ray diffraction (XRD) patterns of the samples were conducted on an X'Pert Pro X-ray diffractometer with Cu K_α radiation (λ = 0.1542 nm) under a voltage of 40 kV and a current of 40 mA. Fourier transform infrared spectra (FTIR) were measured on a Nicolet 6700 FT-IR spectrometer.

Thermogravimetric analysis (TGA, Pyris 1) was performed under air flow from 100 to 800 °C at a heating rate of 10 °C min^{-1}. X-ray photoelectron spectroscopy (XPS) analyses were made with a VG ESCALAB 220I-XL device. All XPS spectra were corrected using the C1s line at 284.5 eV and curve fitting was accomplished using XPS Peak 4.1 software. The Brunauer–Emmett–Teller (BET) specific surface area was measured using a Belsorp-max surface area detecting instrument by N_2 physisorption at 77 K. The electrical conductivity of the prepared samples was tested using a 4-Point Probes Resistivity Measurement System (RTS-8).

2.5. Electrochemical measurements

The electrochemical measurements were carried out in 2025 coin cells assembled in an argon-filled glovebox (M. Braun Inertgas Systems Co. Ltd) with concentrations of moisture and oxygen below 0.1 ppm. Pure lithium foil was used as the counter electrode and a polypropylene film (Celgard-2400) was used as the separator. The electrolyte consisted of a solution of 1 M $LiPF_6$ in ethylene carbonate (EC)/dimethyl carbonate (DMC)/diethyl carbonate (DEC) (1 : 1 : 1 by volume). The flexible GCNF, WS_2/CNF and WS_2/GCNF hybrid membranes were directly used as working electrodes without adding any polymer binders or conductive additives. Therefore, the specific capacities of these hybrid membranes were calculated based on their total mass. By comparison, the bare WS_2 electrodes were prepared by a slurry coating procedure. The slurry consisted of WS_2, carbon black and poly(vinylidene fluoride) dissolved in *N*-methyl-2-pyrrolidinone (NMP) at a weight ratio of 8 : 1 : 1. The as-prepared slurry was pasted on pure copper foil and dried at 80 °C under vacuum. For clarification, the specific capacity of the bare WS_2 electrode was calculated based on the weight of WS_2, excluding carbon black and poly (vinylidene fluoride). The mass loading density of the active material on the WS_2/GCNF electrode was calculated to be about 1.6–2.2 mg cm^{-2}. Cyclic voltammetry (CV) curves were collected on a CHI660D electrochemical workstation (Chenhua Instruments Co. Ltd) in the potential range from 0.01 to 3.0 V at a scan rate of 0.1 mV s^{-1}. The galvanostatic discharge–charge and rate-performance tests under different current densities were performed in the voltage range from 0.01 to 3.0 V at room temperature using a CT2013A cell test instrument (LAND Electronic Co. Ltd). The electrochemical impedance spectroscopy (EIS) was measured in the frequency range from 100 kHz to 0.01 Hz with an AC voltage amplitude of 5.0 mV.

3. Results and discussion

3.1. Structure and morphology of WS_2/GCNF hybrid membranes

As shown in Fig. 2a, the electrospun CNFs had an average diameter of 250–350 nm, a smooth surface without any defects and they were interconnected with each other to form a unique 3D nanofiber network (Fig. S1, see ESI†). In order to further improve the electrical conductivity of CNF, highly conductive graphene sheets were employed as a "conductive sheath" to wrap every single carbon nanofiber. It can be seen that the surface of graphene-wrapped carbon nanofibers (GCNF) become rough and wrinkled due to the wrapping of edge-curled graphene sheets (Fig. 2b and c). The TEM image (Fig. 2d) and cross-sectional FESEM images (Fig. S2†) of GCNF membranes unambiguously confirm the successful wrapping of graphene sheets on every individual carbon nanofiber, even including those in the internal portion of GCNF membranes. It is the hydrogen bond between amino groups of pre-oxidized PAN (oPAN) nanofibers and oxygen-containing groups of graphene oxide (GO) sheets that realize the synthesis of the GCNF hybrid membrane. On the one hand, PAN nanofiber membranes are pre-oxidized to introduce amino groups into PAN chains, which can hinder the nanofibers from melting in the subsequent carbonization process.[28] In comparison with that of PAN membranes, the FTIR spectrum of oPAN membranes (Fig. 2e) shows the emergence of three new peaks located at 1591, 1255 and 790 cm^{-1}, corresponding to the C=N, C–C and C–N stretching vibration and =C–H out-of-plane wagging vibrations, respectively.[28] These results verify the introduction of amino groups in oPAN nanofibers during the pre-oxidation process. On the other hand, the TEM image of GO sheets (Fig. S3†) shows that the exfoliated GO sheets are slightly scrolled on sheet edges and their lateral size are in the range from several hundred nanometers to a few micrometers. The AFM observation of GO sheets (Fig. S4, see ESI†) displays that the thickness of single-layered GO sheets is about 1.0–1.1 nm, revealing that large amounts of oxygen-containing groups are introduced onto the GO sheets during the Hummers oxidation process.[29] Intriguingly, the electrospun oPAN membranes and GO sheets are able to self-assemble with each other in aqueous media, resulting in hierarchical structures whereby every oPAN nanofiber was fully wrapped by GO sheets. The appearance of C=O (1723 cm^{-1}), C–OH (1218 cm^{-1}) and C–O (1050 cm^{-1}) groups of GO sheets in the FTIR spectrum of GO/oPAN membranes (Fig. 2e), as well as the presence of characteristic diffraction peak of GO (2θ = 10.2°) in the XRD pattern of GO/oPAN membranes (Fig. 2f), both strongly confirm the co-existence of GO sheets and oPAN nanofibers in the GO/oPAN membranes.[30] Then, GO/oPAN membranes were converted into GCNF membranes under calcination, where GO sheets were reduced to graphene and oPAN nanofibers were carbonized into CNFs. Notably, the resulting GCNF membranes possess good mechanical flexibility (inset of Fig. 2b) and significantly enhanced electrical conductivity (27.6 S m^{-1}) in comparison with that of the CNF membranes (1.8 S m^{-1}) and those of other graphene/CNF composites reported elsewhere. Considering the above results, GCNF membranes with 3D porous architecture, large specific surface area, good mechanical flexibility and excellent electrical conductivity are promising carbonaceous matrixes to construct hierarchical nanocomposites.

By utilizing GCNF membranes as a template, flexible WS_2/GCNF hybrid membranes were facilely prepared *via* a one-step solvothermal reaction. WS_2 nanosheets are *in situ* grown on the surface of GCNF nanofibers (Fig. 3), and the growth of WS_2 nanosheets can be readily controlled by adjusting the concentrations of $(NH_4)_2WS_4$ solutions. As displayed in Fig. S5 (see ESI†), the size and loading amount of WS_2 nanosheets on the GCNF nanofibers clearly increases with increasing concen-

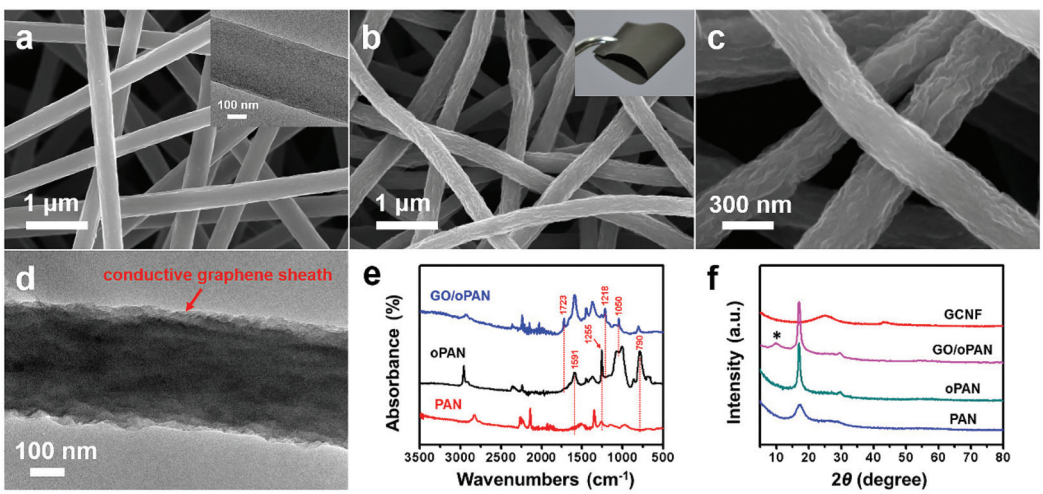

Fig. 2 Characterization of GCNF membrane with conductive graphene sheath wrapping the carbon nanofibers. FESEM and TEM images of (a) CNF and (b–d) GCNF membranes. (e) FTIR spectra and (f) XRD patterns of PAN, oPAN and GO/oPAN membranes. The inset of (b) is the digital photograph of the flexible GCNF membrane.

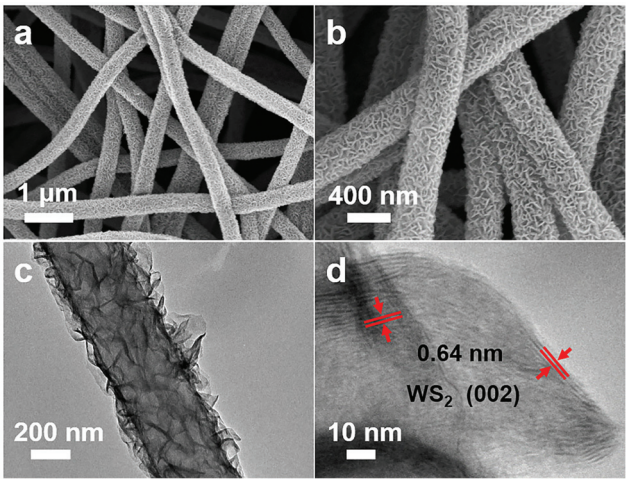

Fig. 3 Microstructure of WS_2/GCNF-2 hybrid membrane. (a, b) FESEM images, (c) TEM and (d) HRTEM images of WS_2/GCNF-2 nanofibers.

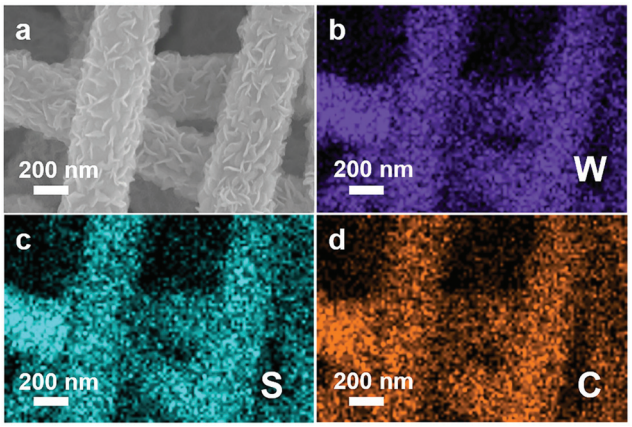

Fig. 4 (a) FESEM image of WS_2/GCNF-2 hybrid membrane and the corresponding EDX mapping of (b) tungsten, (c) sulfur and (d) carbon elements.

trations of $(NH_4)_2WS_4$. Only small WS_2 flakes were evenly scattered on the carbon nanofibers of the WS_2/GCNF-1 hybrid membrane (Fig. S5c†), while a thick layer of large-sized WS_2 nanosheets and spherical WS_2 agglomerates were formed on WS_2/GCNF-3 nanofibers (Fig. S5d†). As for the WS_2/GCNF-2 membrane, the optimized amount of WS_2 nanosheets were uniformly and perpendicularly anchored on the surface of GCNF nanofibers (Fig. 3c), and the lateral size of WS_2 nanosheets were in the range of 100–200 nm. The HRTEM image (Fig. 3d) reveals that WS_2 nanosheets exhibit the typical lamellar structure with an interlayer spacing of 0.64 nm and a thickness of about 3–6 nm, corresponding to 5–10 sandwiched S–W–S layers. Based on the TGA results (Fig. S6, see ESI†), the weight ratios of WS_2 in the WS_2/GCNF hybrid membranes can be calculated from the residual fractions of the WS_2/GCNF samples, and the weight ratios of WS_2 were 54.8%, 74.6% and 88.3% in the WS_2/GCNF-1, WS_2/GCNF-2 and WS_2/GCNF-3 hybrid membranes, respectively. Furthermore, the EDX elemental mapping images of WS_2/GCNF-2 membranes (Fig. 4) reveal the corresponding distribution of tungsten, sulfur and carbon elements, further verifying the successful preparation and homogeneous dispersion of WS_2 nanosheets on GCNF nanofibers. Derived from the 3D porous nanofiber networks and hierarchical nanostructures, the specific surface area (198.6 $m^2\ g^{-1}$) of WS_2/GCNF-2 hybrid membrane calculated from BET analysis (Fig. S7, see ESI†) was significantly larger than that of bare WS_2 nanosheets (7.3 $m^2\ g^{-1}$), which was favorable for effective diffusion of lithium ions throughout the whole electrode structure to ensure sufficient contact with electrode materials.[31] Besides, the morphological compatibility between two-dimensional WS_2 nanosheets and graphene sheets can greatly increase the electrical contact areas for the rapid transfer of lithium ions and electrons across the interfaces. The morphology of the WS_2/CNF hybrid membranes with different contents of WS_2 nanosheets were also investigated (Fig. S8, see ESI†), which were slightly different from those of WS_2/GCNF hybrid membranes. In sharp contrast, bare WS_2 nanosheets prepared without CNF or GCNF membranes severely aggregate into larger spherical agglomerates (Fig. S9, see ESI†), implying the significance of nanofiber membrane templates for effectively dispersing WS_2 nanosheets.

The WS_2/GCNF-2 electrode demonstrated the best electrochemical performance as a binder-free anode for LIBs, and we thus focused investigations on the optimized WS_2/GCNF-2 hybrid membrane in this work. From the XRD analysis of the WS_2/GCNF-2 membrane (Fig. 5a), four diffraction peaks at 2θ = 14.3°, 33.6°, 39.7° and 59.4° were observed, which could be indexed to the (002), (100), (103) and (110) planes of WS_2 (JCPDS 08-0237), respectively. Moreover, the broad (002) diffraction peak of GCNF could also be observed in the XRD

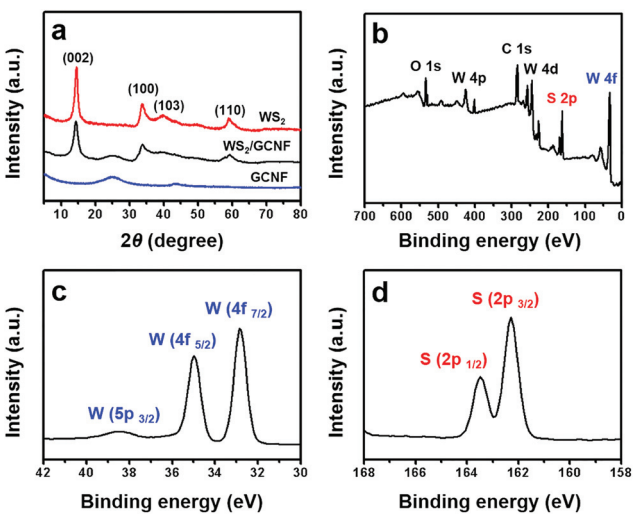

Fig. 5 Characterization of WS_2/GCNF-2 hybrid membrane. (a) XRD patterns, (b) XPS survey spectrum, high resolution (c) W 4f spectrum and (d) S 2p spectrum.

pattern of the WS_2/GCNF-2 hybrid membrane, confirming the co-existence of crystalline WS_2 nanosheets and GCNF nanofibers. The surface electronic state and composition of the WS_2/GCNF-2 hybrid membrane were further investigated by XPS analysis. The survey scan revealed the co-existence of W, S, C and O elements in the hybrid membranes (Fig. 5b). The high-resolution W 4f spectrum shows characteristic peaks located at 32.8, 35.1 and 38.5 eV corresponding to W $4f_{7/2}$, W $4f_{5/2}$ and W $5p_{3/2}$ binding energies, respectively, indicating the dominance of W(IV) in the WS_2/GCNF-2 hybrid membrane (Fig. 5c).[32] From the high resolution S 2p spectrum (Fig. 5d), two peaks at 162.3 eV and 163.5 eV could be observed, which were attributed to S $2p_{3/2}$ and S $2p_{1/2}$ orbitals of divalent sulfide ions (S^{2-}), respectively.[33] These results were in good agreement with those reported previously for WS_2, further verifying the successful synthesis of WS_2 nanosheets grown onto GCNF nanofibers. Besides this, the C1s peak intensities of oxygen-containing functional groups (–C–O and –C═O groups) greatly decreased for the WS_2/GCNF-2 hybrid membrane in comparison with GO sheets (Fig. S10, see ESI†), suggesting that the graphene sheath of GCNF nanofibers was highly reduced after the calcination process.[34] Thus, remarkably enhanced electrical conductivity of GCNF nanofiber membranes was achieved and this lead to efficient electron transport across the interfaces for fast lithiation/delithiation of the electrochemically active WS_2 nanosheets.

3.2. Electrochemical performance of WS_2/GCNF hybrid membranes

Without adding any polymer binders or conducting additives, the flexible self-standing WS_2/GCNF hybrid membranes were directly used as binder-free anode materials to evaluate their electrochemical performance for LIBs. Cyclic voltammetry (CV) tests were performed to reveal the electrochemistry of the lithiation/delithiation process of WS_2/GCNF hybrid membranes (Fig. 6a). In the initial cycle, a strong reduction peak at 0.57 V was observed, which could be ascribed to the conversion reaction of Li^+ with WS_2 nanosheets to form metallic W nanoparticles embedded in the Li_2S matrix.[35] The first anodic scan displayed a strong peak located at 2.32 V, corresponding to the oxidation of Li_2S into S, which was consistent with those characteristics reported previously for the bare WS_2 electrode.[36] In subsequent cycles, the reduction peak at 0.57 V disappeared and two new peaks at 1.76 V and 1.95 V were observed, which could be ascribed to the multistep conversion of S with Li^+ to the formation of Li_2S.[37] The as-formed W nanoparticles did not alloy with lithium, which can facilitate the charge transfer and offer additional interfacial lithium storage sites.[38] CV curves of the subsequent cycles overlapped, indicating excellent structural stability and lithium storage reversibility. Fig. 6b shows the galvanostatic charge and discharge curves of the WS_2/GCNF-2 hybrid membrane at a constant current density of 0.1 A g^{-1}. The potential plateau located at 0.7 V in the initial discharge curve was in accordance with the CV results, representing Li^+ intercalation into layered WS_2 and conversion into the Li_2S phase and W nanoparticles. The

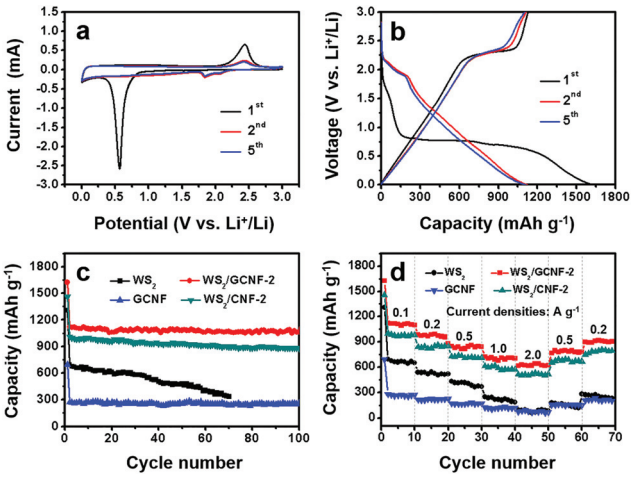

Fig. 6 Electrochemical performance of the WS_2/GCNF anodes. (a) CV curves and (b) galvanostatic discharge–charge curves of the WS_2/GCNF-2 anode in the 1st, 2nd and 5th cycles. (c) Cycling performance of WS_2, GCNF, WS_2/CNF-2 and WS_2/GCNF-2 anodes at a current density of 0.1 A g^{-1}. (d) Rate performance of WS_2, GCNF, WS_2/GCNF-2 and WS_2/CNF-2 anodes at various current densities.

potential plateau at about 1.8 V in the subsequent discharge curves as well as the potential plateau located at 2.3 V in the charge curves were attributed to the reversible conversion reactions of S with Li^+ to Li_2S, which also agrees well with the CV curves. Notably, the initial discharge and charge capacities of the WS_2/GCNF-2 electrode were 1624.3 and 1128.2 mA h g^{-1} respectively, which were significantly higher than those (1305.6 and 693.4 mA h g^{-1}) of the WS_2 electrode. These results could be attributed to the highly conductive pathways provided by GCNF nanofiber membranes and the effective dispersion of WS_2 nanosheets, which can greatly facilitate the rapid transport of electrons and the insertion/extraction of lithium ions into layered WS_2. In addition, the insulating and electrochemically inert binders used for preparing WS_2 electrodes severely decreased the overall lithium storage capacity, while the binder-free WS_2/GCNF-2 membrane can avoid this problem and ensure direct access to active materials by lithium ions with no resistance from binders.[39]

The cycling performances of WS_2, GCNF and WS_2/GCNF hybrid membranes at a current density of 0.1 A g^{-1} are shown in Fig. 6c. The GCNF membrane manifests excellent cycling stability, but its reversible capacity is merely about 250 mA h g^{-1}. Contrarily, the WS_2 electrode displays severe capacity fading, whose specific capacity dramatically decreases to 336.2 mA h g^{-1} after 70 cycles, owning to their serious aggregation and pulverization during the cycling process. By comparison, the WS_2/GCNF-2 electrode delivers significantly improved electrochemical performance with a high initial charge capacity of 1128.2 mA h g^{-1} and retains 1068.5 mA h g^{-1} after 100 cycles. Among all the WS_2/GCNF electrodes, the WS_2/GCNF-2 electrode delivered the highest reversible capacity after 100 cycles (Fig. S11†), which can be ascribed to the optimized amount of WS_2 nanosheets grown on the conduc-

tive GCNF membranes as well as the enhanced electrical contact and charge transfer between WS_2 nanosheets and GCNF nanofibers. Similarly, the WS_2/CNF-2 electrode also exhibited the highest specific capacity after 100 cycles among all the WS_2/CNF electrodes (Fig. S12†). Notably, the WS_2/GCNF-2 electrode exhibited much higher reversible capacity than the WS_2/CNF-2 electrode, which could be attributed to the conductive graphene sheath of GCNF nanofibers. The graphene sheath provided highly conductive pathways to ensure efficient transport of electrons for fast lithiation/delithiation of WS_2 nanosheets. Additionally, except for the initial several cycles, the Columbic efficiency of the WS_2/GCNF-2 electrode (Fig. S13, see ESI†) was almost 100% during the entire cycling process. The post-mortem FESEM observation of the WS_2/GCNF-2 electrode after long-term discharge–charge cycle tests (Fig. S14, see ESI†) revealed that the structural integrity and hierarchical surface of the WS_2/GCNF-2 hybrid membrane were still maintained, though WS_2 nanosheets were inevitably converted into W nanoparticles and Li_2S phase.[40] This strongly confirmed that the GCNF nanofiber played a significant role in mitigating the volumetric expansion of WS_2 nanosheets, thus leading to remarkable electrochemical cyclic stability of the WS_2/GCNF-2 electrode upon long-term cycling.

The rate capabilities of bare WS_2 and WS_2/GCNF-2 electrodes were further investigated under various current densities (Fig. 6d). The specific capacity of the WS_2 electrode faded to less than 80 mA h g^{-1} as the current density increased to 2 A g^{-1}, and only regained 229 mA h g^{-1} when the current density decreased back to 0.2 A g^{-1}. In sharp contrast, the WS_2/GCNF-2 electrode exhibited a high reversible capacity of 624 mA h g^{-1} as the current density increased to 2 A g^{-1}, and regained 910 mA h g^{-1} when the current density changed back to 0.2 A g^{-1}. The specific capacities of GCNF and WS_2/CNF-2 electrodes were 80 and 495 mA h g^{-1} when the current density increased to 2 A g^{-1}, and regained 214 and 802 mA h g^{-1} when the current density decreased back to 0.2 A g^{-1}, respectively. The significantly enhanced rate performance of WS_2/GCNF-2 hybrid membranes could be ascribed to rapid charge transfer between WS_2 nanosheets and GCNF nanofibers that mainly derived from the highly conductive pathways provided by the graphene sheath. This was further verified by the EIS measurements of WS_2, WS_2/CNF and WS_2/GCNF-2 electrodes (Fig. S15, see ESI†). Generally, the Nyquist plot consisted of a semicircle in the high-frequency region and a straight line in the low-frequency region, corresponding to the charge transfer resistance and ion diffusion resistance in the electrode, respectively.[41] It can be clearly seen that the WS_2/GCNF-2 electrode displayed a much smaller semicircle diameter at high frequencies and a more vertical line at low frequencies compared with those of the WS_2 and WS_2/CNF electrodes, illustrating its greatly decreased resistance for charge transfer and ion diffusion. These results directly confirmed that the GCNF nanofibers were able to provide an enhanced transfer rate of electrons during the lithiation/delithiation process, thus resulting in remarkably improved electrochemical performance for the WS_2/GCNF-2 electrode.

4. Conclusions

In summary, we have developed an innovative and efficient approach to fabricate a flexible GCNF membrane with electrospun CNF wrapped by conductive graphene sheets; and then, hierarchical WS_2/GCNF hybrid membranes of WS_2 nanosheets uniformly grown on GCNF nanofibers were prepared as high-performance anodes for LIBs. Benefiting from the synergetic effect of GCNF nanofibers and WS_2 nanosheets, the optimized WS_2/GCNF hybrid membrane with 3D porous structure greatly enhanced the electrical conductivity and structural integrity, and exhibited a high reversible capacity of 1128.2 mA h g^{-1} at a current density of 0.1 A g^{-1} and outstanding cycling stability with 95% capacity retention after 100 cycles. This work, with encouraging results, highlights the great potential of the GCNF membrane, derived from the effective combination of an electrospun CNF core and conductive graphene sheath, and this novel WS_2/GCNF hybrid membrane, with excellent electrochemical performance, could be further explored as a promising anode materials for next-generation LIBs. Moreover, such an efficient approach to prepare conductive GCNF membranes can provide a new pathway for the large-scale production of various functional GCNF-based nanomaterials for advanced energy storage and conversion.

Acknowledgements

The authors are grateful for the financial support from the National Natural Science Foundation of China (51125011, 51373037 and 51433001).

Notes and references

1 A. S. Arico, P. Bruce, B. Scrosati, J. M. Tarascon and W. Van Schalkwijk, *Nat. Mater.*, 2005, **4**, 366–377.
2 F. Y. Cheng, J. Liang, Z. L. Tao and J. Chen, *Adv. Mater.*, 2011, **23**, 1695–1715.
3 P. G. Bruce, B. Scrosati and J. M. Tarascon, *Angew. Chem., Int. Ed.*, 2008, **47**, 2930–2946.
4 J. Lee, C. Jo, B. Park, W. Hwang, H. I. Lee, S. Yoon and J. Lee, *Nanoscale*, 2014, **6**, 10147–10155.
5 C. L. Tan and H. Zhang, *Chem. Soc. Rev.*, 2015, **44**, 2713–2731.
6 H. S. S. R. Matte, A. Gomathi, A. K. Manna, D. J. Late, R. Datta, S. K. Pati and C. N. R. Rao, *Angew. Chem., Int. Ed.*, 2010, **49**, 4059–4062.
7 S. H. Choi, S. J. Boo, J. Lee and Y. C. Kang, *Sci. Rep.*, 2014, **4**, 5755.
8 D. H. Youn, C. Jo, J. Y. Kim, J. Lee and J. S. Lee, *Electrochim. Acta*, 2015, **295**, 228–234.
9 D. Y. Chen, W. X. Chen, L. Ma, G. Ji, K. Chang and J. Y. Lee, *Mater. Today*, 2014, **17**, 184–193.
10 Y. Liu, W. Wang, H. B. Huang, L. Gu, Y. W. Wang and X. S. Peng, *Chem. Commun.*, 2014, **50**, 4485–4488.

11 D. Y. Chen, G. Ji, B. Ding, Y. Ma, B. H. Qu, W. X. Chen and J. Y. Lee, *Nanoscale*, 2013, **5**, 7890–7896.
12 K. Shiva, H. S. S. R. Matte, H. B. Rajendra, A. J. Bhattacharyya and C. N. R. Rao, *Nano Energy*, 2013, **2**, 787–793.
13 Y. Miao, Y. P. Huang, L. S. Zhang, W. Fan, F. L. Lai and T. X. Liu, *Nanoscale*, 2015, **7**, 11093–11101.
14 Y. C. Du, X. S. Zhu, L. Si, Y. F. Li, X. S. Zhou and J. C. Bao, *J. Phys. Chem. C*, 2015, **119**, 15874–15881.
15 G. W. Huang, H. Liu, S. P. Wang, X. Yang, B. H. Liu, H. Z. Chen and M. S. Xu, *J. Mater. Chem. A*, 2015, **3**, 24128–24138.
16 Y. Liu, W. Wang, Y. W. Wang and X. S. Peng, *Nano Energy*, 2014, **7**, 25–32.
17 P. P. Sun, X. Y. Zhao, R. P. Chen, T. Chen, L. B. Ma, Q. Fan, H. L. Lu, Y. Hu, Z. X. Tie, Z. Jin, Q. Y. Xu and J. Liu, *Nanoscale*, 2016, **8**, 7408–7415.
18 A. Abbasi, M. M. Nasef, M. Takeshi and R. Faridi-Majidi, *Chin. J. Polym. Sci.*, 2014, **32**, 793–804.
19 J. Ryu, S. Choi, T. Bok and S. Park, *Nanoscale*, 2015, **7**, 6126–6135.
20 L. S. Zhang, Q. W. Ding, Y. P. Huang, H. H. Gu, Y. E. Miao and T. X. Liu, *ACS Appl. Mater. Interfaces*, 2015, **7**, 22669–22677.
21 L. S. Zhang, Y. P. Huang, Y. F. Zhang, H. H. Gu, W. Fan and T. X. Liu, *Adv. Mater. Interfaces*, 2016, **3**, 1500467.
22 W. M. Lv, J. Y. Xiang, F. S. Wen, Z. Y. Jia, R. L. Yang, B. Xu, D. L. Yu, J. L. He and Z. Y. Liu, *Electrochim. Acta*, 2015, **153**, 49–54.
23 J. H. Kong, C. Y. Zhao, Y. F. Wei and X. H. Lu, *ACS Appl. Mater. Interfaces*, 2015, **7**, 24279–24287.
24 J. X. Zhu, D. Yang, Z. Y. Yin, Q. Y. Yan and H. Zhang, *Small*, 2014, **10**, 3480–3498.
25 Q. Dong, G. Wang, H. Hu, J. Yang, B. Q. Qian, Z. Ling and J. S. Qiu, *J. Power Sources*, 2013, **243**, 350–353.
26 M. K. Dufficy, S. A. Khan and P. S. Fedkiw, *ACS Appl. Mater. Interfaces*, 2016, **8**, 1327–1336.
27 W. S. Hummers and R. E. Offeman, *J. Am. Chem. Soc.*, 1958, **80**, 1339.
28 Q. Y. Wu, H. Q. Liang, M. Li, B. O. Liu and Z. K. Xu, *Chin. J. Polym. Sci.*, 2016, **34**, 23–33.
29 L. S. Zhang, W. Fan and T. X. Liu, *RSC Adv.*, 2015, **5**, 43130–43140.
30 J. Shin, K. Park, W. Ryu, J. Jung and I. Kim, *Nanoscale*, 2014, **6**, 12718–12726.
31 L. S. Zhang, W. Fan, W. W. Tjiu and T. X. Liu, *RSC Adv.*, 2015, **5**, 34777–34787.
32 H. L. Li, K. Yu, H. Fu, B. J. Guo, X. Lei and Z. G. Zhu, *Phys. Chem. Chem. Phys.*, 2015, **17**, 29824–29833.
33 S. S. Zhou, J. N. Chen, L. Gan, Q. Zhang, Z. Zheng, H. Q. Li and T. Y. Zhai, *Sci. Bull.*, 2016, **61**, 227–235.
34 W. Tang, C. X. Peng, C. T. Nai, J. Su, Y. P. Liu, M. V. V. Reddy, M. Lin and K. P. Loh, *Small*, 2015, **11**, 2446–2453.
35 R. J. Chen, T. Zhao, W. P. Wu, F. Wu, L. Li, J. Qian, R. Xu, H. M. Wu, H. M. Albishri, A. S. Al-Bogami, D. Abd El-Hady, J. Lu and K. Amine, *Nano Lett.*, 2014, **14**, 5899–5904.
36 L. Y. Zhou, S. C. Yan, L. J. Pan, X. R. Wang, Y. Q. Wang and Y. Shi, *Nano Res.*, 2016, **9**, 857–865.
37 M. L. Zou, Y. Jiang, M. Wan, M. Zhang, H. Zhu, T. T. Yang and M. L. Du, *Electrochim. Acta*, 2015, **176**, 255–264.
38 S. Yu, J. W. Jung and I. D. Kim, *Nanoscale*, 2015, **7**, 11945–11950.
39 L. S. Zhang, Y. P. Huang, Y. F. Zhang, W. Fan and T. X. Liu, *ACS Appl. Mater. Interfaces*, 2015, **7**, 27823–27830.
40 D. Y. Chen, G. Ji, B. Ding, Y. Ma, B. H. Qu, W. X. Chen and J. Y. Lee, *Nanoscale*, 2013, **5**, 7890–7896.
41 G. C. Huang, T. Chen, W. X. Chen, Z. Wang, K. Chang, L. Ma, F. H. Huang, D. Y. Chen and J. Y. Lee, *Small*, 2013, **9**, 3693–3703.